CHALMERS
UNIVERSITY OF TECHNOLOGY

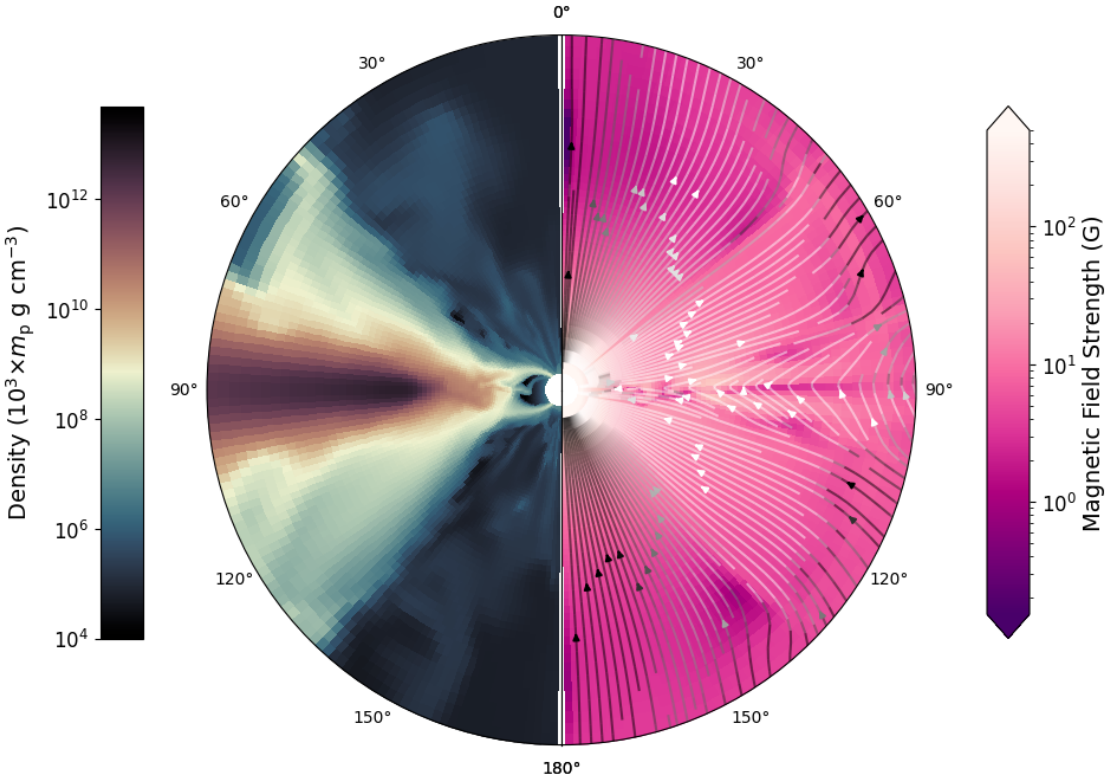

The Dynamics of Inner Protoplanetary Disks and Protostellar Accretion

Insights from Numerical Simulations using PLUTO

Master's Thesis in Master's Programme of Physics

TOMAS THURE

DEPARTMENT OF SPACE, EARTH AND ENVIRONMENT

CHALMERS UNIVERSITY OF TECHNOLOGY
Gothenburg, Sweden 2024
www.chalmers.se

Master's thesis 2024

The Dynamics of Inner Protoplanetary Disks and Protostellar Accretion

Insights from Numerical Simulations using PLUTO

TOMAS THURE

CHALMERS
UNIVERSITY OF TECHNOLOGY

Department of Space, Earth and Environment
Division of Astronomy and Plasma Physics
Chalmers University of Technology
Gothenburg, Sweden 2024

The Dynamics of Inner Protoplanetary Disks and Protostellar Accretion
Insights from Numerical Simulations using PLUTO
TOMAS THURE

Supervisor: Dr. Brandt Gaches, Department of Space, Earth and Environment
Examiner: Prof. Jonathan C. Tan, Department of Space, Earth and Environment

Master's Thesis 2024
Department of Space, Earth and Environment
Division of Astronomy and Plasma Physics
Chalmers University of Technology
SE-412 96 Gothenburg
Telephone +46 31 772 1000

Cover: Density (left) and magnetic field strength (right) plots from PLUTO simulation data, showing the inner region of the protoplanetary disk and accretion onto the protostar.

Typeset in LaTeX
Gothenburg, Sweden 2024

The Dynamics of Inner Protoplanetary Disks and Protostellar Accretion
Insights from Numerical Simulations using PLUTO
TOMAS THURE
Department of Space, Earth and Environment
Chalmers University of Technology

Abstract

In the T Tauri phase of star formation, the central protostar accretes material from the surrounding protoplanetary disk. The magnetic field of the protostar truncates the disk at a certain truncation radius, r_T, from which material is accreted via funnel flows that follow the magnetic field lines. The so-called Hartmann equation for r_T contains a fudge factor ξ that captures the interaction between the magnetic field and the disk. The aim of the report is to investigate where r_T is located for a simulated T Tauri star and see how this compares to theoretical and observed values. Simulations were carried out using the public code PLUTO to solve the conservation laws of magnetohydrodynamics. The modeled protostar had a mass of $1\,M_\odot$ and radius of $3\,R_\odot$. Three different magnetic field strengths were used; 500 G, 1 000 G and 1 500 G. The results show that the average truncation radii throughout the simulations are 6.805×10^{-2}, 8.855×10^{-2} and 9.249×10^{-2} AU with average accretion rates of 1.235×10^{-7}, 1.398×10^{-8} and $3.613 \times 10^{-8}\,M_\odot$ year^{-1} for the different B-fields respectively. The corresponding obtained values of ξ are 1.365, 0.6414 and 0.6970, with the latter two lying in the expected range of 0.5-1 for typical T Tauri stars. The reason for the deviating ξ-value in the 500 G case could not be conclusively determined. It could be that the assumptions of a perfect dipole and free-falling gas made when deriving the Hartmann equation do not hold for weaker magnetic fields. More research is, however, needed to explore this further.

Keywords: T Tauri star, accretion, protoplanetary disk, truncation radius.

Contents

List of Figures

List of Tables

1
Introduction

Since the dawn of time, we humans have been curious about our origin. Looking up at the night sky and wondering why and how our existance came into being, is an integral part of what it means to be human. In the modern age, our horizons have been ever expanding. By using telescopes, we can now explore beyond our familiar Earth and Solar system, towards other solar systems in our Galaxy and beyond. From only knowing about the Earth, Moon, Sun and local planets in ancient times, we now have a much clearer picture of our place in the Universe. Our Sun is only one among many others, separated by the interstellar medium (ISM). The stars visible to the naked eye are all part of our Galaxy, the Milky Way, with the stars, gas and dust concentrated in its magnificent spiral arms and a supermassive black hole residing in the center of the galaxy. The galaxy is only one among an unfathomable number of other galaxies in the Universe.

Although our knowledge and understanding is constantly increasing, there are still many mysteries and unanswered questions left to explore. It is, for example, not fully understood how the Earth and the other planets formed. Since the conditions under which the planets were formed are long gone, it is difficult to draw conclusions about the formation of them by only studying the current Solar system. By the usage of powerful telescopes it is, however, possible to observe planetary systems that are currently being formed. This can give clues about how our own Solar system formed. Furthermore, most of the elements that are found on Earth and that are vital for life, are created inside stars. So to understand our own origin, it is vital to understand the processes of star and planetary formation as well as the environment in which it takes place.

1.1 Star formation

The ingredients to make a star are found in giant clouds of gas in the ISM. These clouds lie mostly in the disk of the Galaxy and mostly consist of molecular hydrogen, H_2 [1]. By mass, the ISM consists of around 70% hydrogen and 28% helium with only 2% consisting of heavier elements [2]. The clouds are enormous in scale as they can be several hundred light years across and weigh up to $10^5\,M_\odot$. The mass is, however, not evenly spread throughout a cloud. Some regions of the clouds can have a density that is a thousand times higher than the average density in the cloud [1]. These so called dense cores are the seeds for making stars.

Within the cloud, there are many forces that are competing against each other. The inward gravitational force is counter-balanced by e.g. gas turbulence, magnetic fields and thermal pressure. One common criterion to determine whether a cloud will collapse or not, is the Jeans instability. It assumes that the gas in the cloud is uniformly distributed in a sphere. If the cloud is perturbed, the gas will compress. With a sufficiently large compression, the gravity from the compressed gas will attract even more mass, thus starting an unreversible inward gravitational collapse [3]. With this criterion, a larger density makes a collapse more probable, while a higher temperature hinders collapse.

At the center of the collapse, mass is gathered into a protostar, which will later develop into a star. During about a hundred thousand years, surrounding gas and dust is accreted onto the protostar at a rate of around one Earth mass every year [1]. At the same time, mass is expelled through bipolar outflow winds originating from the poles of the protostar. Because of conservation of angular momentum, as material falls closer to the central protostar, its rotational velocity increases. Material with low velocity can fall directly onto the protostar while material with higher velocity can settle in orbits around the protostar. The varying velocity of the material makes it settle in orbits of different radii, thus forming a protoplanetary disk.

When the surrounding envelope of dust is depleted and accretion stops, the central object is now considered to be a pre-main-sequence star. This phase lasts for tens of millions of years. During the initial stage, the object is often referred to as a *T Tauri* star, named after a typical example found in the Taurus constellation. At this point, the temperature of the core of the protostar is around 3 000 to 4 000 K, which is hot enough to fuse deuterium atoms and protons into helium-3, a process which releases energy.

As the inward graviational pressure grows ever stronger, it eventually wins over the outward thermal gas pressure, making the protostellar core heat up to around ten million kelvin. This is hot enough to allow four protons to fuse into one helium-4. The onset of this process is what marks the beginning of the main sequence phase of the star's life. This is where the star will spend most of its lifetime and it is the stage at which our Sun is currently in. This stage lasts for billions of years until the star eventually dies.

1.2 Observational motivation

In recent years, the number of detected exoplanets, planets outside our Solar system, has increased drastically. One observatory that has helped with detecting many planets is the *Kepler Space Telescope*. During its active operation between 2009 and 2018, it detected a total of 2 662 exoplanets [4]. One primary objective was to investigate if there are habitable, Earth-like planets close to their stars, within one astronomical unit (au) [5]. Discovering habitable planets is an important step in the search for life beyond Earth, as it provides insight into the abundance of such planets and where to focus the search in future studies. One surprise from

the Kepler survey is the large amount of solar systems with several inner planets with short orbital periods. Most observed exoplanets have a radius between the Earth's and Neptune's and an orbital period less than that of Mercury, our Solar system's innermost planet [6]. The planets of these systems mostly orbit in the same plane, with very little spread in orbital inclination. This suggests that the planets formed from the protoplanetary disk, either by forming directly in the inner disk or by migrating there after forming further out. If the planets formed *in situ*, that is directly where they are observed today without migrating inward, then there must have been material that close to the protostar when the planetary system formed. If there was no gas in the innermost region, that would imply that no planets could have formed *in situ* there. It is thus of interest to understand how close to the protostar that the protoplanetary disk can reach, as it can help explain the occurrence of these exoplanets.

1.3 Protostellar accretion

As the core collapses to a central protostar, a protoplanetary disk forms around it. The reason for the formation of a disk has to do with conservation of angular momentum. As material falls inwards, it will gain a higher velocity. So why does gas accrete onto the protostar instead of remaining in stable orbit in the disk? In order for accretion to occur, the inner region of the disk must transfer some of its angular momentum to the outer region. There are several mechanisms involved in this process, but the most dominant one is thought to be the magnetorotational instability (MRI) [7]. This is a mechanism in which shear in the disk causes tension in the magnetic field lines. The consequence of this is that inner gas elements transfer angular momentum to outer gas elements. This makes the inner gas lose velocity and thus falls into an orbit closer to the protostar. This way, material is transferred inwards to the innermost region of the protoplanetary disk.

Once material is accumulated in the inner regions of the disk, there are two main ways that the gas can accrete onto the actual surface of the protostar. In the absence of or with a very weak stellar magnetic field, the disk can make direct contact with the surface layer of the protostar [8]. In the case of a magnetized star, the star will have a magnetosphere which depletes the gas in its vicinity. The disk is thus truncated at a certain radius and gas is instead accreted along the magnetic field lines. The so-called Hartmann equation describes at which radius the magnetosphere truncates the disk. This radius depends on the stellar magnetic field, B, stellar radius, R, stellar mass, M, and accretion rate, $\dot{M}$, according to

$$r_T \approx 18\xi \frac{B_3^{4/7} R_2^{12/7}}{M_{0.5}^{1/7} \dot{M}_{-8}^{2/7}} R_\odot, \tag{1.1}$$

where $\xi \lesssim 1$ is a dimensionless parameter which depends on specific details of the interaction between the magnetosphere and the disk [9]. In the above equation, the fiducial values are set to be $B = 1$ kG, $R = 2\,R_\odot$, $M = 0.5\,M_\odot$, $\dot{M} = 10^{-8}\,M_\odot$ year^{-1}.

Through computer simulations, it is possible to model an accreting protostar. It is the goal of this report to tweak the stellar magnetic field strength to investigate how this affects the location of the truncation radius. This is then compared to the Hartmann equation to see how well the data from the simulations correspond to the theoretical prediction.

2

Theory

This chapter introduces some theory that is helpful to the understanding of the rest of the report. It gives an introduction to protostellar accretion, truncation radius estimations and a brief summary of the key equations in magnetohydrodynamics.

2.1 α-disk model

In protoplanetary disks, mass and angular momentum is mainly transfered through processes involving turbulence [10]. A common way to treat the turbulence is to assume that the small-scale turbulence that is caused for example by MRI, is acting macroscopically like a true viscosity. In 1973, Shakura & Sunyaev introduced the dimensionless α parameter which embodies this viscosity [11]. In this way, the viscosity can be written as:

$$\nu = \alpha c_s H_P, \tag{2.1}$$

where H_P is the verical pressure scale height of the gas, c_s is the sound speed and $\alpha \leqslant 1$. H_P is defined by:

$$H_P = \frac{c_s}{\Omega_K} \tag{2.2}$$

where $\Omega_K = \sqrt{\frac{GM_*}{r^3}}$ is the Keplerian angular velocity. With this definition, the viscocity can also be written as:

$$\nu = \frac{\alpha c_s^2}{\Omega_K}. \tag{2.3}$$

2.2 Accretion

Many typical features of disk accretion are exhibited by protostars; magnetospheric funneling of gas, jets and outflows [9]. The main idea of protostellar accretion is that through some mechanism, material is transported inwards through the disk to a radius of a few stellar radii. At this point, the disk is truncated by the stellar magnetic field. The material is guided along the field lines and falls inward to the star via so-called funnel flows. This picture assumes that the stellar magnetic field is strong enough. It is thought that low mass stars exhibit this kind of magnetospheric accretion, while intermediate to high mass stars have significantly weaker magnetic

fields and thus no magnetospheric accretion.

In 1979, Ghosh & Lamb [12] developed a model for a magnetically threaded disk, which can be applied to T Tauri stars [13]. In this model, the disk transmits torque to the star. At a certain radius, the magnetic field will remove angular momentum from the disk at a higher rate than the internal viscous stress. When this occurs, the gas will no longer remain in stable orbit, and it will fall onto the protostar.

In the following derivation, it is assumed that both the disk and star lie at $z = 0$. The star has radius R_*, mass M_*, angular velocity Ω_* and accretion rate $\dot{M}$. The disk rotates at the Keplerian speed Ω_K. Assume that the magnetic field from the protostar is a dipole according to:

$$B_z(r) = -\frac{\mu}{r^3} \tag{2.4}$$

where μ is the dipole moment.

The Alfvén radius for spherical accretion can be found by equating ram pressure and the pressure of the magnetic field [14]. Another interpretation is that radial kinetic energy equals the magnetic energy [13]. The ram pressure can be written as:

$$\frac{\rho v_{ff}}{2} = \frac{\dot{M}}{8\pi r^2}\sqrt{\frac{2GM_*}{r}} \tag{2.5}$$

where v_{ff} is the free-falling speed. The magnetic field pressure can be written as:

$$P_M = \frac{\mu^2}{8\pi r^6}. \tag{2.6}$$

By equating these two expression, the Alfvén radius can be defined as:

$$r_A \equiv \mu^{4/7}\dot{M}^{-2/7}(2GM_*)^{-1/7}. \tag{2.7}$$

With $\mu = B_z r^3$, Equation 2.7 can be written as:

$$r_A = \left(\frac{B_z^4 r^{12}}{2GM_*\dot{M}^2}\right)^{1/7}. \tag{2.8}$$

It can be shown that the truncation radius is of the same order as the Alfvén radius, such that $r_T = \xi r_A$. This finally gives the Hartmann equation. With the assumed fiducial values found in Section 1.3, the truncation radius can be written as:

$$r_T \approx 18\xi\frac{B_3^{4/7}R_2^{12/7}}{M_{0.5}^{1/7}\dot{M}_{-8}^{2/7}}R_\odot. \tag{2.9}$$

where $\xi \lesssim 1$ is a dimensionless parameter which depends on specific details of the interaction between the magnetosphere and the disk. While it is difficult to obtain a theoretical prediction of how large ξ is, most previous research estimates it to be around 0.5-1 for classical T Tauri stars [15] [16].

2.3 Magnetohydrodynamics

The simulations used in this report are governed by a set of equations which are numerically solved at each time step. These equations are a part of magnetohydrodynamics (MHD). In order to understand the gas dynamics in protoplanetary disks and the simulations, it is therefore important to understand MHD and its underlying principles and equations. MHD describes the interaction between magnetic fields and electrically conducting fluids [17].

In the ideal case the equations are given by:

$$\frac{\partial \rho}{\partial t} + \nabla \cdot (\rho \mathbf{v}) = 0, \tag{2.10}$$

$$\rho \frac{d\mathbf{v}}{dt} = \mathbf{J} \times \mathbf{B} - \nabla p, \tag{2.11}$$

$$\frac{d}{dt}\left(\frac{p}{\rho^{\gamma}}\right) = 0, \tag{2.12}$$

$$\mathbf{E} + \mathbf{v} \times \mathbf{B} = 0, \tag{2.13}$$

$$\nabla \times \mathbf{E} = -\frac{\partial \mathbf{B}}{\partial t}, \tag{2.14}$$

$$\nabla \times \mathbf{B} = \mu_0 \mathbf{J}, \tag{2.15}$$

$$\nabla \cdot \mathbf{B} = 0, \tag{2.16}$$

where ρ is the mass density, $\mathbf{v}$ is the velocity, p is the pressure, $\mathbf{E}$ is the electric field, $\mathbf{B}$ is the magnetic field and $\gamma = 5/3$ is the adiabatic index. Equation 2.10 is the mass conservation equation which imposes the condition that the total number of particles is conserved. Equation 2.11 describes the conservation of momentum which has three force components; the magnetic force $\mathbf{J} \times \mathbf{B}$, the pressure gradient force ∇p and the inertia force $\rho \frac{d\mathbf{v}}{dt}$. Equation 3.3 describes the energy evolution which is assumed to be adiabatic with $\gamma = 5/3$. Equation 2.13 is Ohm's law which in the ideal case assumes that the gas is a perfect conductor. It is this assumption that implies the "ideal" name to ideal MHD. The main terms that are neglected are the electrical resistivity and Hall effect. The three equations 2.14, 2.15 and 2.16 collectively make up Maxwell's equations.

One important parameter used in MHD is the plasma β. It is defined as the ratio of plasma pressure to the magnetic pressure [17]. With this definition, it can be written as:

$$\beta \equiv \frac{p}{B^2/2\mu_0} \tag{2.17}$$

where μ_0 is the vacuum permeability.

3
Method

This chapter describes the methods that were implemented to generate the results. It describes how the PLUTO code was used and which assumptions, initial- and boundary conditions that were used. A description is given to how the generated data was processed and visualised in various ways in order to compare the results to theoretical predictions.

3.1 Overview of simulation setup

Three different simulations were conducted, with the difference between them being the strength of the stellar magnetic field. The choices of stellar magnetic fields were $B = 500$ G, $B = 1\,000$ G and $B = 1\,500$ G. It has been found through observations that most T Tauri stars have B-fields from around 500 G to 2 kG or slightly above [18]. The values were thus chosen to cover a sizable portion of this range. The simulations were carried out for a protostar of mass $M_* = 1\,M_\odot$ and radius of $R_* = 3\,R_\odot$. The simulations were all run with the same timesteps and for the same duration of 69.26 days in physical time. This corresponds to roughly 30 stellar rotations.

3.2 PLUTO code

To study the protoplanetary disk, the public code PLUTO was used [19]. The PLUTO code is written in the C programming language and is used to simulate a protostar and its interaction with the protoplanetary disk. The code is very adaptable as it can solve a variety of systems of conservation laws in one, two or three dimensions. The grid on which the simulations are run can also be modified to use Cartesian, cylindrical or spherical coordinates. The grid can also be completely uniform or stretched, meaning that the resolution is higher in certain regions of the disk. In addition, a variety of numerical methods are available to do the time stepping and to solve the conservation laws. The choices of the above mentioned alternatives are discussed below. The choosen boundary and initial conditions are also described.

3.2.1 General setup

In the PLUTO code, the MHD physics module was choosen. The HLL solver was used with the Lagrange multiplier divergence cleaning method. The MHD equations

are evolved in time with Runge-Kutta integration of second order. The equations that were solved in each step, are the following conservation laws:

$$\frac{\partial \rho}{\partial t} + \nabla \cdot (\rho \mathbf{v}) = 0 \tag{3.1}$$

$$\frac{\partial \mathbf{m}}{\partial t} + \nabla \cdot \left[\mathbf{m}\mathbf{v} - \mathbf{B}\mathbf{B} + I \left(p + \frac{\mathbf{B}^2}{2} \right) \right]^T = -\rho \nabla \Phi + \rho \mathbf{g} \tag{3.2}$$

$$\frac{\partial \mathbf{B}}{\partial t} + \nabla \times (c\mathbf{E}) = 0 \tag{3.3}$$

$$\frac{\partial (E_t + \rho\Phi)}{\partial t} + \nabla \cdot \left[\left(\frac{\rho \mathbf{v}^2}{2} + \rho e + p + \rho \Phi \right) \mathbf{v} + c\mathbf{E} \times \mathbf{B} \right] = \mathbf{m} \cdot \mathbf{g} \tag{3.4}$$

where $\mathbf{v}$ is the gas velocity, ρ is the mass density, $\mathbf{m} = \rho\mathbf{v}$ is the momentum density, $\mathbf{B}$ is the magnetic field, p is the thermal pressure of the gas, $\mathbf{g} = -\nabla\Phi$ is the acceleration vector [16] and E_t is the total energy density which can be expressed as:

$$E_t = \rho e + \frac{\mathbf{m}^2}{2\rho} + \frac{\mathbf{B}^2}{2}. \tag{3.5}$$

Here e indicates the specific internal energy which is related to the equation of state [19]. In the simulations, the ideal equation of state was used, such that the internal energy can be written as:

$$\rho e = \frac{p}{\gamma - 1} \tag{3.6}$$

where $\gamma = 5/3$ is the adiabatic index. $\mathbf{g}$ is the gravitational acceleration vector and Φ is the gravitational potential prom the protostar. The expression for the potential is:

$$\Phi = \frac{GM_*}{r}. \tag{3.7}$$

In Equation 3.3, $\mathbf{E}$ is the electric field which is defined by:

$$c\mathbf{E} = -\mathbf{v} \times \mathbf{B} + \frac{\eta}{c} \cdot \mathbf{J}, \tag{3.8}$$

where c is the speed of light, η is the resistivity and $\mathbf{J} = c\nabla \times B$ is the induced current. In the ideal case, $\eta = 0$.

In the code itself, the equations are solved in dimensionless units. This is to avoid very large or small numbers that could otherwise arise in cgs units. So dimensions for base quantities have to be provided from which all other variables derive their respective dimensional scaling. The dimensions are given by $v_0 = 1$ km/s, $L_0 = 1$ AU and $\rho_0 = 10^3\, m_p/\mathrm{cm}^3$, m_p is the proton mass in grams. From these, all other units are derived, for example time $t_0 = L_0/v_0$ and magnetic field $B_0 = v_0\sqrt{4\pi\rho_0}$.

3.2.2 Initial conditions

Several initial conditions had to be chosen before running the simulations. In the following description, (r, θ, ϕ) is used to denote spherical coordinates and (R, z) to denote cylindrical coordinates in two dimensions. The surface density profile of the disk is then given by:

$$\Sigma(R) = \Sigma_0 \left(\frac{R}{R_0}\right)^{-1} e^{R/R_{\max}}, \tag{3.9}$$

where Σ is the surface density of the gas, R is the cylindrical radius. R_0 is the normalization radius, choosen to be $R_0 = 10$ AU and $R_{\max} = 40$ AU, is the maximum radius. The density is:

$$\rho = \frac{\Sigma(R)}{\sqrt{2\pi}h} e^{-z^2/h^2}, \tag{3.10}$$

where $h = c_s/\Omega$ is the scale hight of the disk, c_s is the sound speed and Ω is the angular velocity. The tangential velocity is given by the Keplerian velocity:

$$v_\phi = \sqrt{\frac{GM_*}{R}}. \tag{3.11}$$

The initial core is set with the following density profile:

$$\rho_{\text{env}} = \rho_{0,\text{env}} \left(\frac{r}{50 \text{ AU}}\right)^{-1.5}. \tag{3.12}$$

Σ_0 and ρ_0 are calculated such that the mass ratios between the protostar and the disk and protostar and core are $\frac{M_{\text{disk}}}{M_*} = 0.175$ and $\frac{M_{\text{core}}}{M_*} = 0.1$.

It is furthermore assumed that there is an initial magnetic field in the disk. The vector potential of the field is defined by:

$$A_\phi = \begin{cases} \frac{2B_1}{3-a} r^{-(a-1)/2} & \text{for } r > R_* \\ 0 & \text{for } r \leqslant R_*, \end{cases} \tag{3.13}$$

where $B_1 = \sqrt{2p_1/\beta}$, β is the ratio between thermal and magnetic pressure. p_1 is the pressure at 1 AU. In the simulations, values of $a = m = 1.5$ were used.
The temperature is initially set to vary as:

$$T(R) = T_0 \left(\frac{R}{R_0}\right)^{-0.5}. \tag{3.14}$$

The gravitational potential of the protostar is given by:

$$\Phi(r) = \frac{GM_*}{r}. \tag{3.15}$$

The protostar produces a background magnetic field which is defined by the magnetic vector potential:

$$A_* \hat{\phi} = \frac{B_* R_*^3}{r^2}. \tag{3.16}$$

3.2.3 Geometry and grid

The simulations are run on a grid that is 128×128 cells in size. In the radial direction, the 128 cells are spaced logarithmically from the protostellar surface out to 1 AU. This means that the grid resolution is higher close to the protostar than in the outer region. In the θ-direction, the 128 cells are uniformly spaced in the interval $[10^{-2}, \pi - 10^{-2}]$. The reason for the margin of 10^{-2} is to avoid numerical instabilities at the poles at $\theta = 0$ and $\theta = \pi$. The chosen grid gives a maximum and minimum resolution of around 5×10^{-4} AU and 3×10^{-2} AU respectively.

3.2.4 Viscosity and Resistivity

In the simulations, the viscosity is included through the α parameter such that the shear viscosity is:

$$\nu_s = \alpha c_s h, \tag{3.17}$$

where c_s is the sound speed. An α parameter value of $\alpha = 10^{-3}$ was chosen for all the simulations.

3.2.5 Boundary conditions

At the outermost radial boundary, it is assumed that there is outflow, but no inflow. It is also assumed that there is axi-symmetric θ boundary condition. The inner boundary is more complicated. It is assumed that the protostar is a perfect conductor, which determines the poloidal component of the velocity and magnetic field. The magnetic field components follow an outflow boundary condition.

3.2.6 Heating and cooling

Both continuum and atomic line cooling is included for gas with temperatures $10^4 < T < 10^9$ K and the protostar also heats the gas via X-rays. Line cooling is included through a tabulated cooling rate and was calculated by using the `ChiantiPy` package for collisional ionization equilibrium and solar abundances. The X-ray heating is included as a flux throgh a cell at distance r:

$$F_X = \frac{L_X}{4\pi r^2}, \tag{3.18}$$

where L_X is an X-ray luminosity which was set to be $L_X = 10^{29}$ erg s^{-1}.

3.2.7 Output files and visualisations

There are many output formats that PLUTO can generate. In this project, the chosen output was in the form of VTK (Visualization ToolKit) files [19]. Using this format, at a given snapshot, all output variables are stored within the same output file. The data analysis and plotting was done using Python scripts. To read the data in the VTK files, the pyPLUTO tool was used. pyPLUTO is included in the default PLUTO software.

3.3 Data analysis

This section describes how the data was analysed after the simulations were run. Quantities such as the truncation radius and accretion rate were calulated and visualised in various ways.

3.3.1 Truncation radius

There are various ways to calculate the truncation radius given the data that PLUTO generates. This section describes how the truncation radius was defined and calculated from each output file. Firstly, a wedge around the midplane of the disk was constructed. From the total grid that has dimensions 128×128, the wedge was considered to be the full radius of the disk but only ± 5 indices around the midplane.

One output variable in the output file is the velocity in θ-direction, v_θ. In the wedge, this velocity is a good approximation of the velocity in z-direction, perpendicular to the disk. In the disk, the gas above and belove the midplane are expected to have similar but opposite velocities. This means that in the wedge, the average vertical velocity is expected to average to zero. Whithin the truncation radius, however, the asymetric flow of gas means that the average velocity is expected to be non-zero and vary quite a lot. According to this logic a definition of truncation can be made based on how v_θ varies in the wedge.

At each radial index, the standard deviation, σ, of v_θ was calculated in that wedge segment using `numpy.std()`. In Figure 3.1 the standard deviation is plotted as a function of radius for the $B = 1\,000$ G case at 69.26 days. The graph varies significantly in the inner region but is stable close to zero in the rest of the disk. By making these plots for all three simulations and at different times, it could be concluded that throughout the simulations the standard deviation of v_θ is always stable around a value of zero from 0.2 AU and outward.

The average of the σ values from 0.2 to 1 AU, σ_μ, was then calculated. The truncation radius is lastly defined to be the first radius going inward from 0.2 AU at which σ of v_θ reaches $5\sigma_\mu$. Figure 3.2 shows σ plotted as a function of radius for the $B = 1\,000$ G case at 69.26 days in a log-log plot with the calculated truncation radius indicated. This definition guarantees that the truncation radius is found within 0.2 AU. Ignoring this condition could give a truncation radius that is obviously located within the disk if random asymitries in velocity well within the disk can trigger the $5\sigma_\mu$ threshold.

The calculated truncation radius was also plotted on top of visualisations of the disk to check if the location of the truncation radius is reasonable. Figure 3.3 shows density and temperature plots for the same snapshot for the $B = 1\,000$ G case, with the truncation radius indicated. As can be seen from the density plot, the truncation radius is located close to where the density drops significantly, especially around the midplane.

The described method to calculate the truncation radius is used for a single snapshot of the data, but the same procedure was repeated for each output file. In this way, each snapshot corresponds to a single truncation radius.

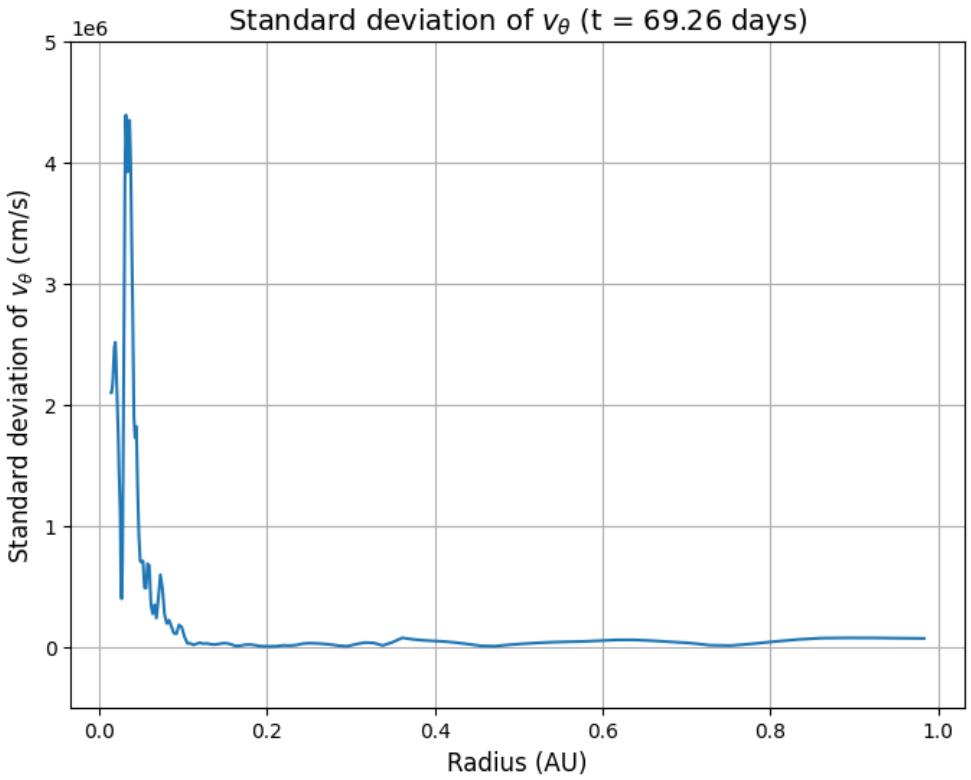

Figure 3.1: The standard deviation of v_θ within each wedge segment, plotted against radius from 0 to 1 AU. The snapshot is for the $B = 1\,000$ G case at 69.26 days. In the innermost region of the wedge, the value spikes, while it remains close to zero further out.

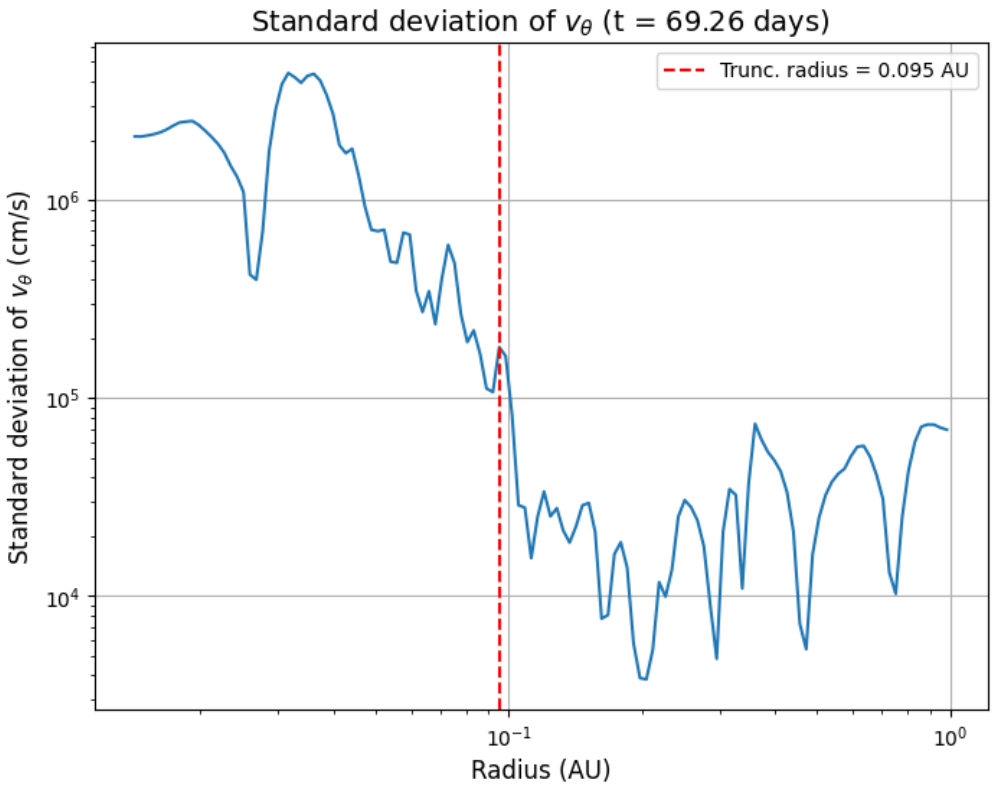

Figure 3.2: The standard deviation of v_θ within each wedge segment, plotted against radius from 0 to 1 AU in a log-log scale. The snapshot is for the $B = 1\,000$ G case at 69.26 days. The calculated truncation radius is indicated with the red dotted line. It is located where the graph first reaches a value 5 times the average from 0.2 to 1 AU

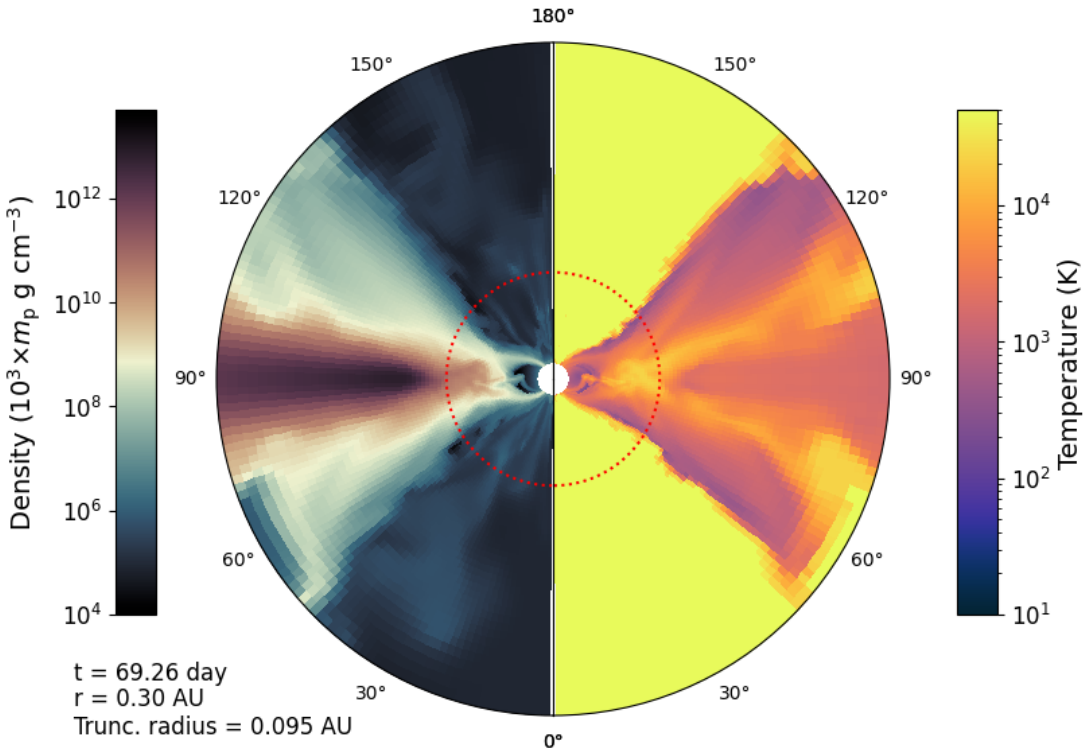

Figure 3.3: Temperature (right) and density (left) plots for the full angular range and radius up to 0.3 AU. The snapshot is for the $B = 1\,000$ G case at 69.26 days. The truncation radius is indicated at 0.095 AU, close to where the midplane density drops significantly.

3.3.2 Accretion rate

The accretion rate is not directly given as an output variable from the VTK files, so it has to be calculated for each snapshot. The equation used to calculate the accretion rate for a cell at the protostellar surface with surface element dA is:

$$\dot{m}_i = \rho v_r dA. \tag{3.19}$$

The total accretion rate is just:

$$\dot{m} = \frac{2\pi}{d\Phi} \sum_i \dot{m}_i, \tag{3.20}$$

where axisymmetric accretion is assumed and $d\Phi = 1$ in code units.

3.3.3 Pressure

In order to better understand the dynamics of the inner regions, pressures in the disk were calculated and plotted. The three pressures that were calculated are thermal, ram and magnetic pressure. The thermal pressure is given directly as an output variable from the PLUTO code. The ram and magnetic pressures were calculated as:

$$P_{\text{ram}} = v_r^2 \rho, \quad P_{\text{mag}} = \frac{B^2}{2}. \tag{3.21}$$

These pressures were plotted as averages in wedge segments of ± 10 indices around the midplane. This was done for the final snapshot of each simulation.

3.3.4 Visualisation

The data was visualised in several ways. Firstly, the accretion rate was plotted as a function of time for all three simulations. Figure 3.4 shows the $B = 1\,000$ G simulation as an example. It can be seen from the plot that the accretion rate is initially unstable. After the initial spike, the accretion rate stabilizes. The other two simulations exhibit similar initial spikes in accretion rate. To avoid these initial instabilities, the first 10% of data points were cut out from each simulation and the remaining 90% were used in the subsequent analysis. Since the simulations all consist of 4 000 output VTK files, the number that was actually used is 3 600.

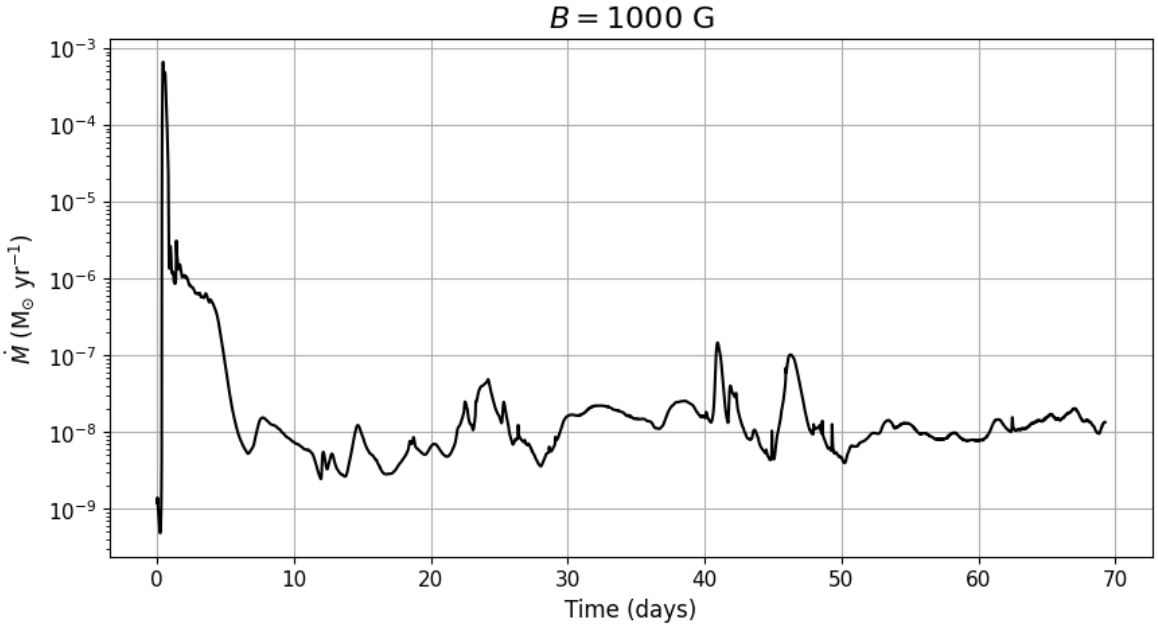

Figure 3.4: Accretion rate in log scale plotted against time for the entire duration of the $B = 1\,000$ G simulation. Note the large initial spike in accretion rate which is removed before further data analysis.

To help visualise the spread in accretion rate, histograms were first constructed for each simulation. They indicate how many of the 3 600 accretion rate points fall within bins that are uniformly distributed on a logarithmic scale between the lowest and highest accretion rate in the set. The number of bins were set to 20 for all histograms.

Then the truncation radii were plotted against accretion rate for each simulation. A power law function was also fitted to the points to investigate how close it corresponds to the Hartmann equation which predicts $r_T \propto \dot{m}^{-2/7}$. The power law

equation is $y = ax^b$ and the fitting was done using `scipy.optimize.curve_fit()` in `Python`. So the power law fitting function takes x- and y-data as input and returns optimized values for a and b using the least squares method. The value of b can then be compared to the Hartmann prediction. The error in b is calculated as:

$$\sigma_b = \sqrt{\mathrm{Var}[b]}, \tag{3.22}$$

where $\mathrm{Var}[b]$ is given by the diagonal element corresponding to the b variable in the covariance matrix generated by the fitting function. This error therefore corresponds to one standard deviation from the optimal curve.

Instead of plotting each simulation separately, the datapoints for all simulations were combined. However, since the simulations use different values of B, it is not very meaningful to simply plot r_T over $\dot{m}$. In order to be able to compare the results with the Hartmann equation, another approach is needed. The Hartmann equation predicts:

$$r_T \propto \frac{B^{4/7}}{\dot{m}^{2/7}} = \left(\frac{B^2}{\dot{m}}\right)^{2/7}. \tag{3.23}$$

The plotted quantity was therefore chosen to be r_T against $\frac{B^2}{\dot{m}}$. In this case the fitted power law curve should give $b = 2/7$ according to the Hartmann equation. This was done for all $3\,600 \times 3 = 10\,800$ data points combined. It was also done with only three points, one for each simulation, where each point is the arithmetic mean of the datapoints within that simulation.

4
Results & Discussion

This chapter presents the results that were generated through the method described in Chapter 3. In the table below, Table 4.1, a summary of the results is presented. It shows the arithmetic mean of the truncation radii and accretion rates for each simulation. From these mean values, numerical values of the ξ parameter can be obtained, which are presented in the far right column. The obtained values for the $B = 1\,000$ G and $B = 1\,500$ G cases of $\xi = 0.6414$ and $\xi = 0.6970$ respectively, are within the expected range of 0.5-1. The result for these two cases is thus considered to follow the expected outcome. For the 500 G case, however, the obtained value is $\xi = 1.365$ which is above the expected range. This indicates that there is some physics involved that is not present in the other two cases or that the assumptions made when deriving the Hartmann equation do not hold for such low B-field strengths. The following subsections go into more details of the obtained results. In Section 4.3 pressure plots are presented as a first step in explaining the deviating results obtained for the $B = 500$ G case.

B (G)	r_T (AU)	$\dot{m}$ ($M_\odot$ year^{-1})	ξ
500	6.805×10^{-2}	1.235×10^{-7}	1.365
1000	8.855×10^{-2}	1.398×10^{-8}	0.6414
1500	9.249×10^{-2}	3.613×10^{-8}	0.6970

Table 4.1: Arithmetic mean values of r_T, $\dot{m}$, and ξ for the three different magnetic field strengths.

4.1 Accretion rate

In order to visualise the interval of accretion rates and which ones are most probable for a given simulation, histograms of accretion rates were constructed for all three simulations. They were all constructed in the same way as described in Section 3.3.4. The histograms for all three cases are shown in Figure 4.1. The figure shows that for the $B = 500$ G case, there is a lot of spread in accretion rate throughout the simulation. The lowest accretion rate is down to almost $10^{-9}\,M_\odot$ year^{-1} while the highest accretion rate is over $10^{-6}\,M_\odot$ year^{-1}. The accretion rates with the highest frequency can be found around $10^{-7}\,M_\odot$ year^{-1}.

The histogram for the $B = 1\,000$ G case shows that the range of accretion rates is significantly more narrow than for the $B = 500$ G case. The lowest value reaches down

to almost $10^{-9}\,M_\odot$ year^{-1} while the highest accretion rate is just above $10^{-7}\,M_\odot$ year^{-1}. The vast majority of accretion rates have values of around $10^{-8}\,M_\odot$ year^{-1} or slightly lower.

The histogram for the $B = 1\,500$ G case shows that this simulation has the most narrow spread of accretion rate out of the three simulations. Only a small portion of the data points lie below $10^{-8}\,M_\odot$ year^{-1} or above $10^{-7}\,M_\odot$ year^{-1}. Within this range, there is not a clear clustering of data points or clear indications of a normal distribution as can be found in the other two cases.

Figure 4.2 shows truncation radius plotted agains accretion rate for all three simulations. On top of the data points, a red fitted line is shown with the exponent and its error indicated. There is also a green dotted line which shows the Hartmann exponent of -2/7 which intersects the fitted line at its midpoint. Note that this is just for comparison of the slopes in the log-log plot, as no consideration to the prefactor is taken.

In the $B = 500$ G case, the figure shows that there is no visual indication of a clear power law relation between the points. This is further supported by the quite flat fitted curve with an exponent of -0.008. Note the large error in this case, 0.0028. In the $B = 1\,000$ G case, the figure shows that there is no visual indication of a clear power law relation between the points. This case also has a flat fitted curve with an exponent of -0.013 with an error of 0.0042. In the $B = 1\,500$ G case, the fitted curve has an exponent of 0.066 with an error of 0.0024.

From the figure, it can be concluded that within each simulations there is no clear power law relation between the data points. None of the exponents are close to the expected Hartmann exponent -2/7 with the $B = 1\,500$ G case even having a positive exponent.

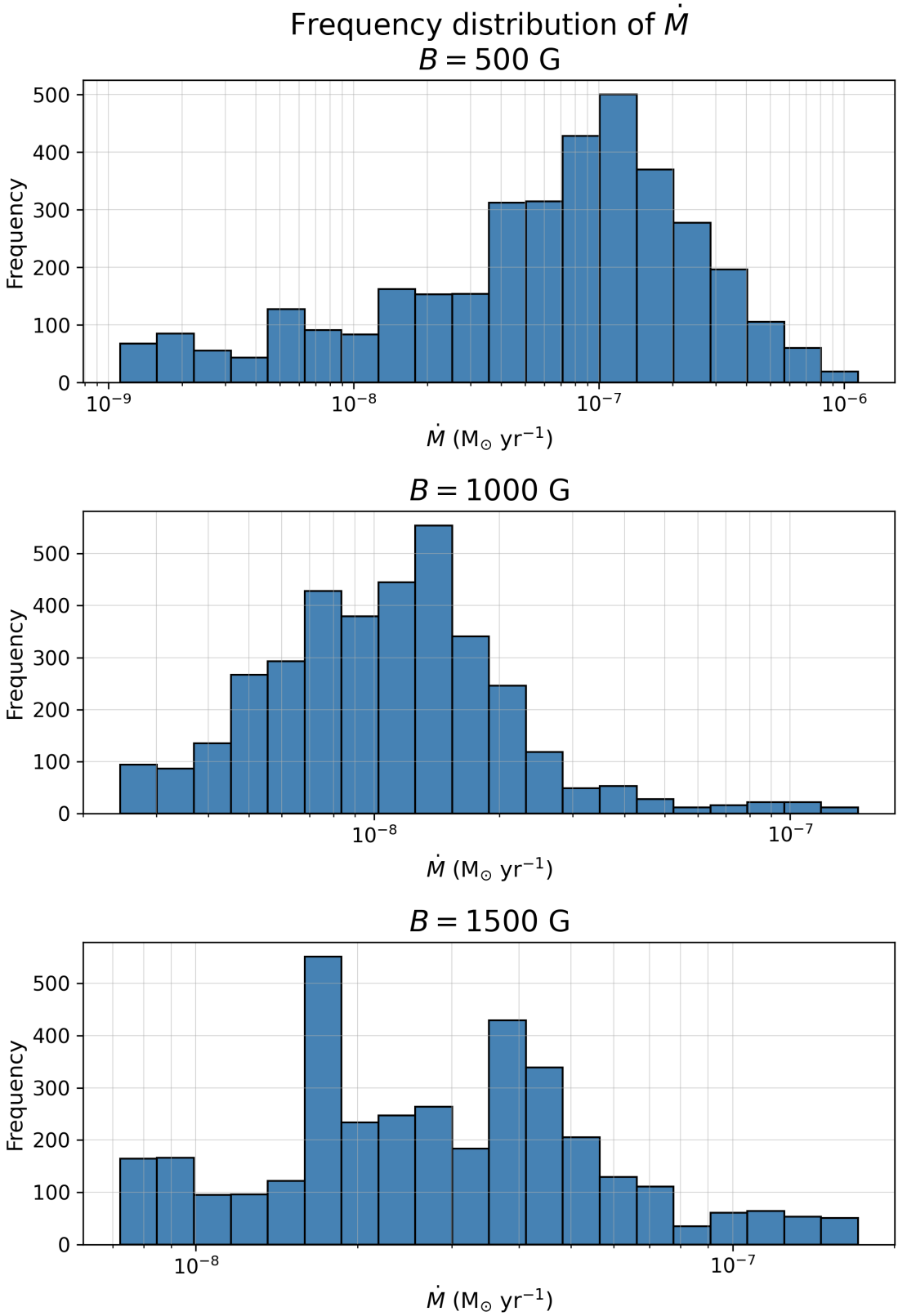

Figure 4.1: Frequency distribution of accretion rate, $\dot{m}$, for the $B = 500$ G (top), $B = 1\,000$ G (middle) and $B = 1\,500$ G (bottom) simulations. For each plot, 3 600 data points and 20 bins were used, with the bins being uniformly distributed on the log scale between the lowest and highest accretion rate.

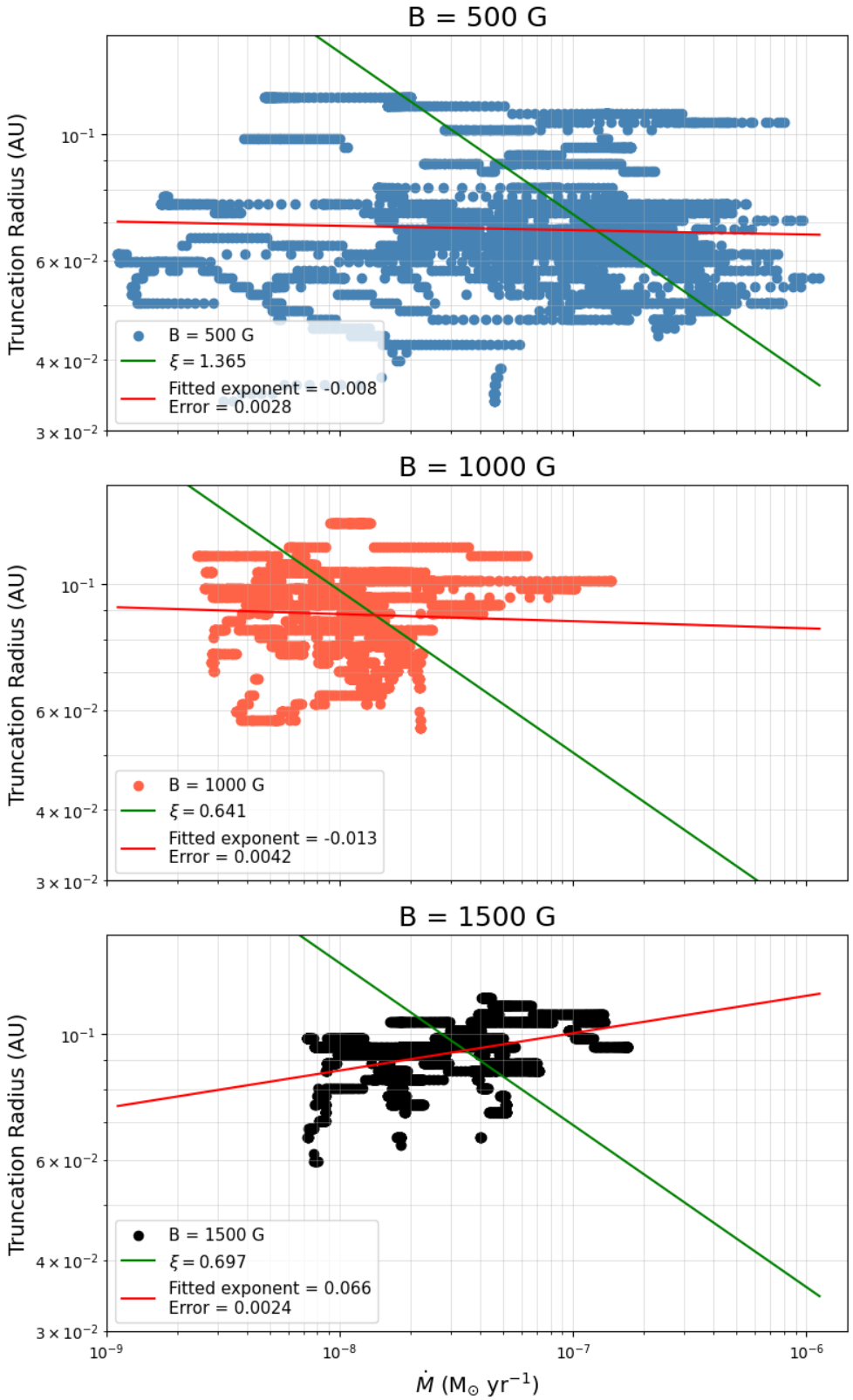

Figure 4.2: The truncation radius, r_T, plotted against accretion rate, $\dot{m}$, for the $B = 500$ G (top), $B = 1\,000$ G (middle) and $B = 1\,500$ G (bottom) simulations. In each plot, the red line is a fitted power law while the green line is the calculated Hartmann truncation radius using the respective values of ξ. Note the shared x- and y-axis scaling of the plots.

4.2 Comparison to Hartmann equation

In order to better compare the data to the Hartmann equation, another approach is needed, as discussed in Section 3.3.4. That is because the truncation radius depends on both the magnetic field and the accretion rate. The comparison can be done by plotting r_T against $\frac{B^2}{\dot{m}}$. Figure 4.3 shows this plot for all 10 800 data points combined. A power law function is fitted through the points with an exponent of 0.059 and an error of 0.0012. In the plot, this is compared to the Hartmann prediction which has an exponent of 2/7. Altough the fitted exponent is positive, it differs substantially from the value of 2/7.

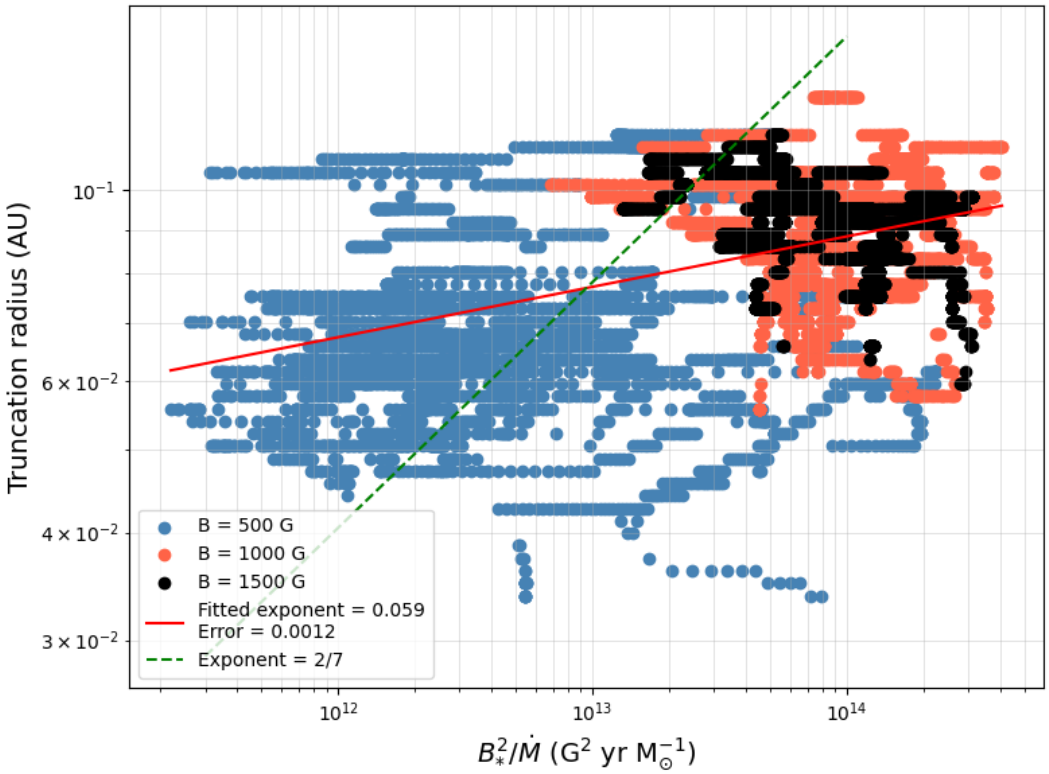

Figure 4.3: The truncation radius, r_T, plotted against $\frac{B^2}{\dot{m}}$ for all three simulations. The red line is a fitted power law while the green dotted line is the overlayed Hartmann prediction for comparison.

In addition, instead of using all points to fit the curve, the arithmetic means of the data points for each of the three simulations were plotted and a curve fitted through them. Figure 4.4 shows this plot with the fitted exponent being 0.145 with an error of 0.0333. Note that the error only incudes the fit through the three points and disregards the fact that the points themselves are the mean of collections of points. The obtained exponent is larger than the one found in Figure 4.3. It is, however, around only half the value of the Hartmann prediction.

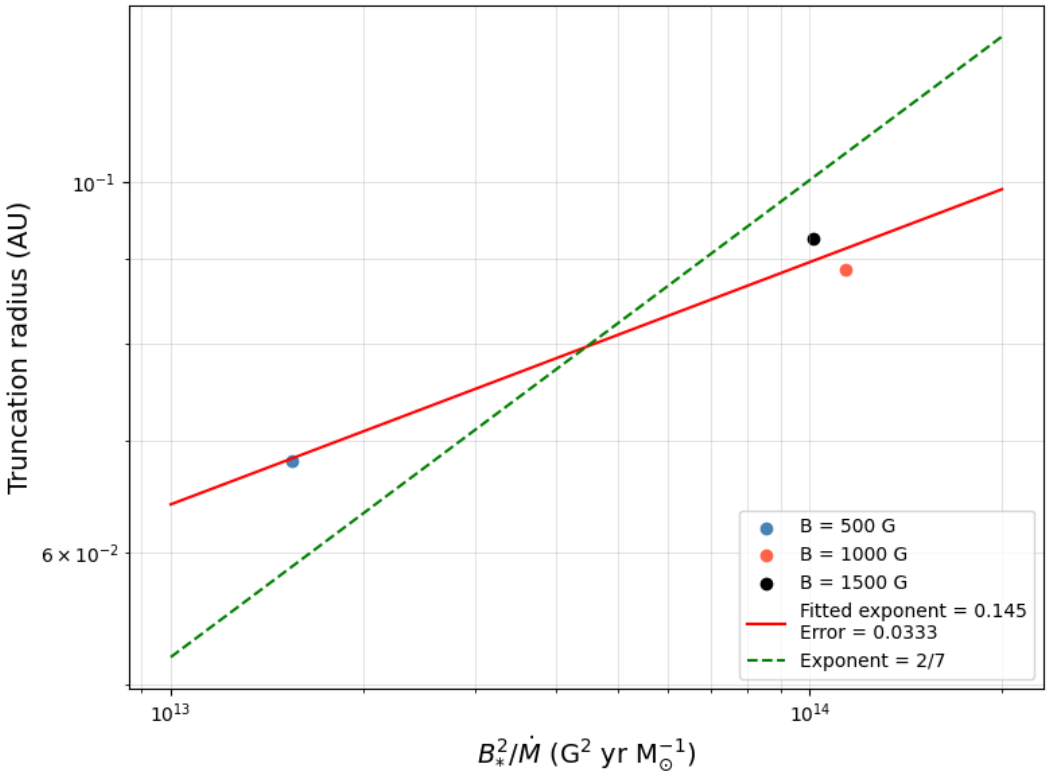

Figure 4.4: The truncation radius, r_T, plotted against $\frac{B^2}{\dot{m}}$ for the arithmetic mean of all three simulations. The red line is a fitted power law while the green dotted line is the overlayed Hartmann prediction for comparison.

4.3 Pressure plots

In order to investigate possible explanations for the deviating behaviour of the $B = 500$ G simulation, plots of the pressure around the midplane were constructed. Figure 4.5 shows ram, magnetic and thermal pressure as a function of radius for each simulation. In each plot, the average and instantaneous truncation radii are also indicated. When deriving the Hartmann equation, it is assumed that the truncation occurs where the ram and magnetic pressures balance. In the figure, that corresponds to the blue and green lines crossing. From the figure it can be seen that the average truncation radius is located roughly where the lines cross, especially in the $B = 1\,000$ G and $B = 1\,500$ G cases. This indicates that the mentioned assumption holds for these B-field strengths. In the $B = 500$ G case, however, there is a wider gap between the two graphs. It can also be noted that the magnetic pressure for quite small radii deviates from the perfect dipole pressure that goes as r^{-6}. This early deviation from a perfect dipole in the $B = 500$ G case could help explain the deviation from the Hartmann prediction, as the assumption of a perfect dipole seems to not hold well in this case. It is, however, difficult to draw conclusions from the pressure graphs. Further research is needed to figure out the physical details that govern the low B-field regime, which assumptions hold and which do not.

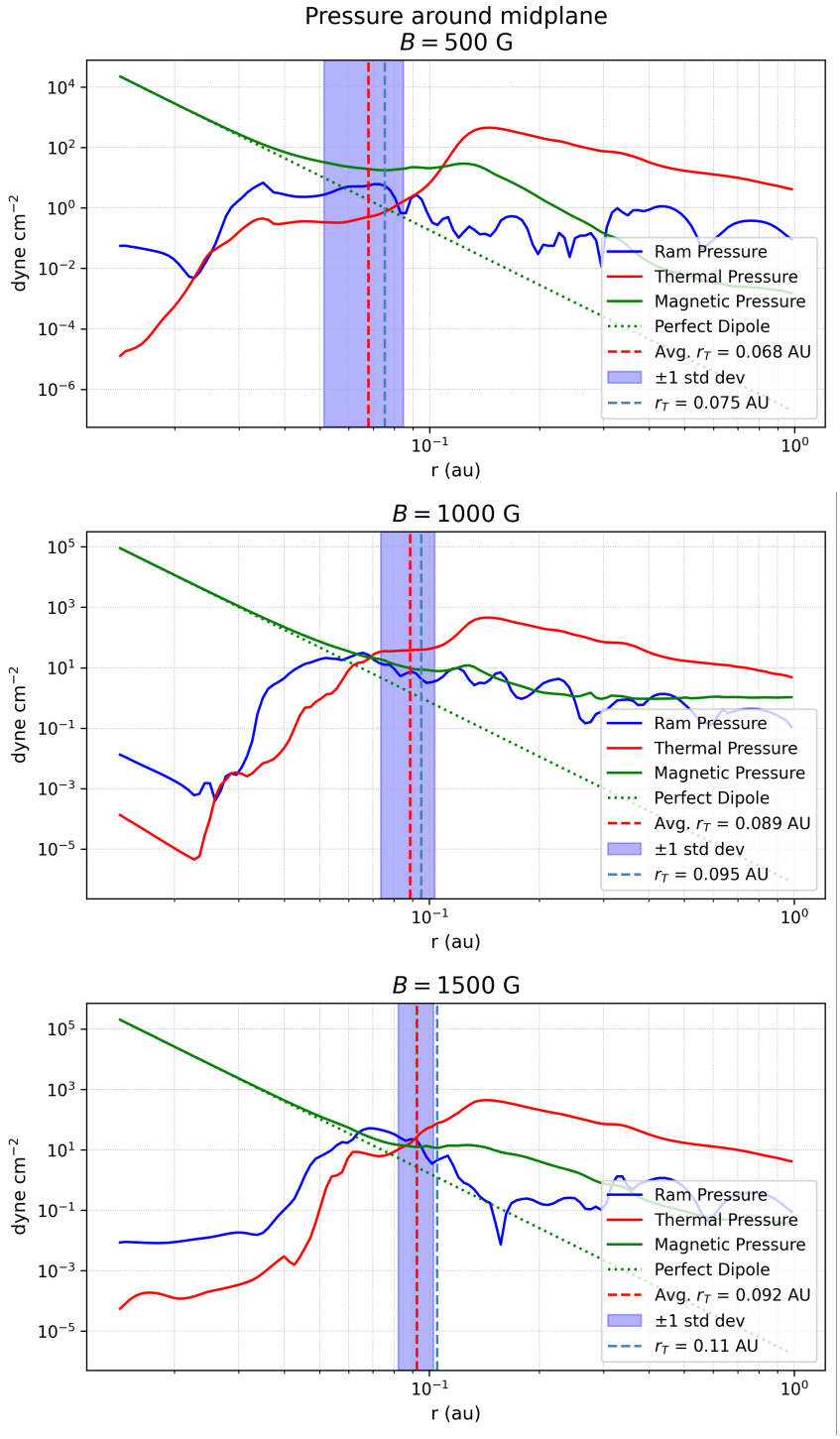

Figure 4.5: Ram pressure (blue solid), thermal pressure (red solid) and magnetic pressure (green solid) plotted against radius for the $B = 500$ G (top), $B = 1\,000$ G (middle) and $B = 1\,500$ G (bottom) simulations at the final snapshot. In each plot, the red dashed line is the average truncation radius with the standard deviation indicated by blue shaded area while the blue dashed line is the instantaneous truncation radius. The green dotted line indicates a perfect magnetic dipole. Note that in the $B = 500$ G case, the magnetic pressure quickly deviates from a perfect dipole.

5
Conclusion

In this project, simulations of a T Tauri star with a surrounding protoplanetary disk were run using the PLUTO code. Three different stellar magnetic fields were used; 500 G, 1 000 G and 1 500 G. From the simulations, the truncation radii and accretion rates were calculated and the results were compared to the Hartmann equation. From the results presented in Chapter 4, it can be concluded that the $B = 1\,000$ G and $B = 1\,500$ G simulations behave as expected. From the mean truncation radii and accretion rates, ξ-values of $\xi = 0.6414$ and $\xi = 0.6970$ respectively were obtained. These values are well within the expected range of around 0.5-1 for T Tauri stars. For the $B = 500$ G case, however, the obtained ξ-value was $\xi = 1.365$ which is above the expected range. There is also much more spread in accretion rate for this case compared to the other two, with the stronger B-field cases having accretion rates clustered around $10^{-8}\,M_\odot$ year^{-1}.

Within each simulation, there is no clear power law relation. Even when normalizing for the different magnetic field strengths, the obtained power law relation is not close to the Hartmann relation. When including all points, the obtained power law exponent is 0.059 and when only considering the average points, the exponent is 0.145, while the expected Hartmann exponent is $2/7 \approx 0.29$.

Pressure plots were also constructed. From the plots, it can be seen that the perfect dipole assumption from the Hartmann equation holds badly for the $B = 500$ G case, possibly explaining the deviating obtained ξ-value. To explain the behaviour fully, however, further investigation is needed. It could be that either the perfect dipole assumption does not hold, the free-fall assumption does not hold, or both. By not including these assumptions, a modified Hartmann equation could be constructed that is valid for the entire range of observed T Tauri stellar magnetic fields. This would improve our knowledge of how accretion onto the protostar and truncation of the protoplanetary disk works for T Tauri stars with weak magnetic fields.

Bibliography

[1] T. Greene, "Protostars," *American Scientist*, vol. 89, no. 4, p. 316, 2001.

[2] B. T. Draine, *Physics of the Interstellar and Intergalactic Medium*. 2011.

[3] A. Choudhuri, *Astrophysics for Physicists*. Astrophysics for Physicists, Cambridge University Press, 2010.

[4] P. G and A. Kumari, "Identification and classification of exoplanets using machine learning techniques," 2023.

[5] N. M. Batalha, "Exploring exoplanet populations with nasa's kepler mission," *Proceedings of the National Academy of Sciences*, vol. 111, p. 12647–12654, July 2014.

[6] W. J. BORUCKI, "Kepler: A brief discussion of the mission and exoplanet results," *Proceedings of the American Philosophical Society*, vol. 161, no. 1, pp. 38–65, 2017.

[7] P. J. Armitage, "Physical processes in protoplanetary disks," 2017.

[8] W. Kley and D. N. C. Lin, "The Structure of the Boundary Layer in Protostellar Disks," , vol. 461, p. 933, Apr. 1996.

[9] L. Hartmann, G. Herczeg, and N. Calvet, "Accretion onto pre-main-sequence stars," *Annual Review of Astronomy and Astrophysics*, vol. 54, p. 135–180, Sept. 2016.

[10] J. E. Pringle, "Accretion discs in astrophysics," , vol. 19, pp. 137–162, Jan. 1981.

[11] N. I. Shakura and R. A. Sunyaev, "Black holes in binary systems. Observational appearance.," , vol. 24, pp. 337–355, Jan. 1973.

[12] P. Ghosh and F. K. Lamb, "Accretion by rotating magnetic neutron stars. III. Accretion torques and period changes in pulsating X-ray sources.," , vol. 234, pp. 296–316, Nov. 1979.

[13] Y.-M. Wang, "Location of the inner radius of a magnetically threaded accretion disk," *The Astrophysical Journal*, vol. 465, p. L111, jul 1996.

[14] J. L. Linsky and M. Güdel, "Exoplanet host star radiation and plasma environment," in *Characterizing Stellar and Exoplanetary Environments*, pp. 3–18, Cham: Springer International Publishing, 2015.

[15] F. Shu, J. Najita, E. Ostriker, F. Wilkin, S. Ruden, and S. Lizano, "Magnetocentrifugally Driven Flows from Young Stars and Disks. I. A Generalized Model," , vol. 429, p. 781, July 1994.

[16] C. Zanni and J. Ferreira, "MHD simulations of accretion onto a dipolar magnetosphere. I. Accretion curtains and the disk-locking paradigm," , vol. 508, pp. 1117–1133, Dec. 2009.

[17] J. P. Freidberg, *Ideal MHD*. Cambridge, England: Cambridge University Press, July 2014.

[18] C. Flores, M. S. Connelley, B. Reipurth, and G. Duchêne, "The effects of starspots on spectroscopic mass estimates of low-mass young stars," *The Astrophysical Journal*, vol. 925, p. 21, Jan. 2022.

[19] A. Mignone, G. Bodo, S. Massaglia, T. Matsakos, O. Tesileanu, C. Zanni, and A. Ferrari, "PLUTO: A Numerical Code for Computational Astrophysics," , vol. 170, pp. 228–242, May 2007.

DEPARTMENT OF SPACE, EARTH AND ENVIRONMENT
CHALMERS UNIVERSITY OF TECHNOLOGY
Gothenburg, Sweden
www.chalmers.se

CHALMERS
UNIVERSITY OF TECHNOLOGY